Anomalous liquid imbibition at the nanoscale: the critical role of interfacial deformations

Shaina Kelly, Carlos Torres-Verdín,* and Matthew T. Balhoff

Department of Petroleum and Geosystems Engineering, The University of Texas at Austin, Austin, TX 78712

Supplementary Information

1. Dynamic Imbibition Example
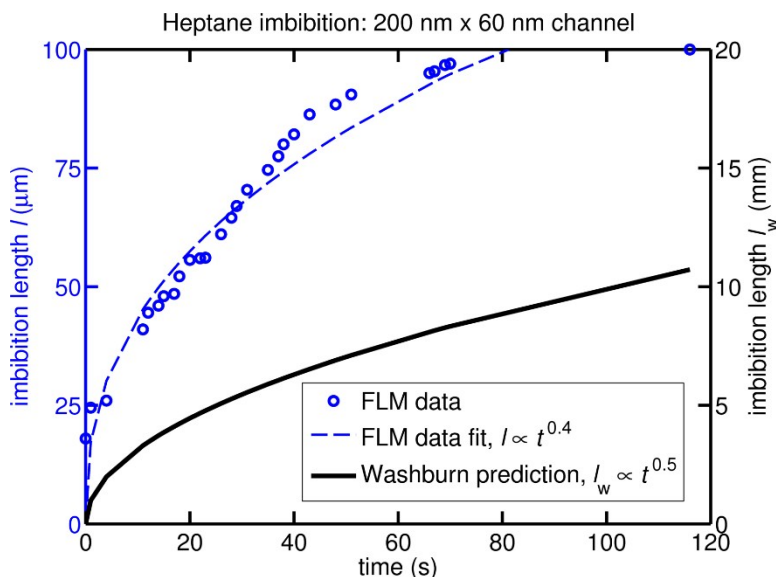
Figure S1. Example of <u>dynamic</u> imbibition data of length-versus-time captured for heptane in a new 200 nm × 60 nm nanochannel. The fluorescent microcopy data (blue points) diverge from the Washburn equation prediction (black line) for this channel size in terms of α and n of the $l = \alpha t^n$ imbibition power law. This dynamic data was captured using the same fluorescence imaging methods used to obtain the static imbibition termination lengths described in the manuscript; this heptane front moved slow enough that capture of dynamic lengths was feasible with manual image acquisition. The termination length of the data is around 100 μm. This data is associated with the imbibition front displayed in Figure 2.A; the third and fourth channels from the right side are both 200 nm × 60 nm in cross-section. Only one front is plotted but the fronts in these two channels had were nearly matching in rate and termination length; i.e. minimal experimental dispersion for this case.

2. Experimental Sensitivity/Dispersion Examples
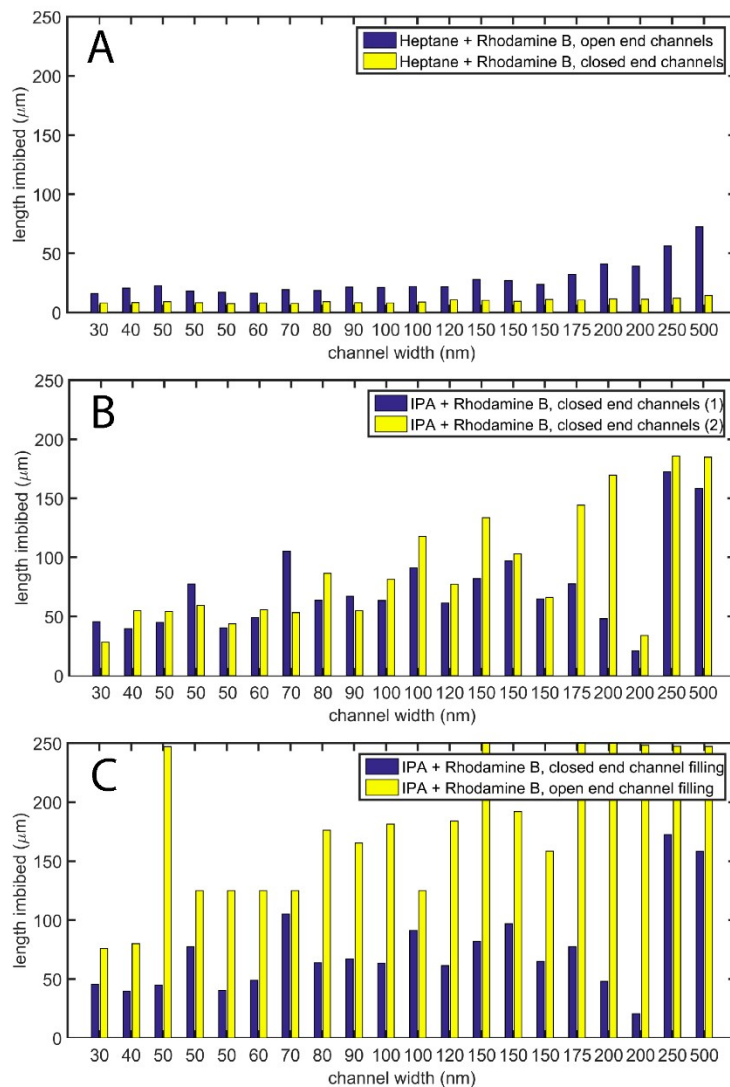
Figure S2. Bar plots of imbibition termination lengths in used chips subject to fouling, mainly by the repeated use of Rhodamine B. (A) and (C) Plots show that heptane and isopropanol (IPA) are sensitive to closed end conditions (the microchannel/nanochannels juncture opposite of the imbibing front is closed off). (B) The haphazard trend in channel termination lengths and general inconsistency between two IPA imbibition runs in the same chip indicate a "struggling" meniscus that is subject to arrest by pinning mechanisms.

3. Background and Theory

Macroscopic Menisci

The Young-Laplace equation stipulates that the curvature, κ, at any point of a conventional, static liquid-gas meniscus is constant and governed by the point's corresponding radii of curvature, R_1 and R_2. Specifically, two perpendicular planes intersect along the surface normal of the chosen point and the intersection of the planes with the meniscus interface produces two space curves with principal radii of

2

curvature and centers of curvature lying on the surface normal vector. The product of the curvature and surface tension, γ, renders the macroscopic capillary pressure, P_c^m, between the two fluids, namely,

$$P_c^m = \gamma \left(\nabla \cdot \overset{\vee}{n} \right) = \gamma \kappa = \gamma \left(\frac{1}{R_1} + \frac{1}{R_2} \right). \quad (S1)$$

Solid-liquid-gas contact angles are approximated by Young's equation, given by

$$\gamma_{sg} = \gamma_{ls} + \gamma_{gl} \cos \theta, \quad (S2)$$

where γ_{sg}, γ_{ls}, and γ_{gl}, are, respectively, the solid-gas, liquid-solid, and gas-liquid interfacial tensions and θ is the "fixed contact angle" boundary condition for the Young-Laplace equation.[1] γ_{gl} is typically referred to as just γ as seen in Eq. S1. For lyophilic ("liquid loving") surfaces such as silica, liquid is the wetting fluid and gas is the non-wetting fluid. The signature hemispherical curvature of a meniscus is a result of molecules near the fluid interface seeking to minimize interaction energy. Again, curvature is assumed to be constant throughout the meniscus. Bulk capillary pressure in a rectangular conduit of dimensions $h \times w$, a firsthand approximation for the geometry of the nanochannels and nano-slits in this work, is then defined as [2] [3]

$$P_c^m = 2\gamma \cos(\theta) \left(\frac{1}{h} + \frac{1}{w} \right). \quad (S3)$$

Molecular Theory of Viscosity

Viscosity, μ, can be summarized as a resistance to flow when a stress or shear is applied that is due to the strength of intermolecular forces between liquid molecules. Liquid viscosity can be estimated with Eyring's theory,[4]

$$\mu = \left(\frac{\delta}{a} \right)^2 \frac{\tilde{N}h}{\tilde{V}} \exp\left(\Delta \tilde{G}_0 / RT \right), \quad (S4)$$

where δ is the distance between molecular layers, a is length of jump a molecule must make to get to a vacant space, $\tilde{N}$ is Avogadro's number, h is the Planck constant, $\tilde{V}$ is liquid molar volume, R is the gas constant, T is temperature, and $\Delta \tilde{G}_0$ is the molar free energy of activation for a molecule to escape from a "cage" of neighbor molecules.

Imbibition

Imbibition is the process where a wetting fluid invades a conduit or pore space occupied by a non-wetting fluid. This process is driven by capillary pressure alone or capillary pressure and the influences of external body forces. In the viscous regime, imbibition can be described by Eq. S5, a quasi-equilibrium expression. Specifically, at the imbibition length, l, the apparent capillary pressure, P_c^a, is in equilibrium with the pressures of the nonwetting and wetting fluids, P_{nw} and P_w, taking into account viscous losses due to imbibition velocity, u, fluid viscosity, μ, conduit permeability or hydraulic conductivity, k, and imbibition length, l, and neglecting the viscous resistance of air, the non-wetting fluid such that

$$P_{nw} = P_l - P_c^a, \quad (S5a)$$

and

$$P_l = P_w - \frac{u\mu l}{k}. \quad (S5b)$$

Thus, a decrease in capillary pressure and/or increase in viscosity results in decreased values of imbibition length and velocity. Setting $u = dl/dt$ in Eq. S5 and solving the resulting differential equation results in the Washburn equation.

Surface Forces

Long-range intermolecular forces or van der Waals forces are the sum of the dipole forces between molecules, including London (dispersion interactions), Keesom (orientation or dipole-dipole interactions), and Debye (induction or dipole-induced dipole interactions) forces. In addition to van der Waals forces, electrostatic (double layer), solvation (or hydration), and structural forces are potential components of the net force or pressure present within thin films or boundary zones at surfaces and interfaces; this net force acting perpendicularly to the interface surface is termed the disjoining pressure.[5] Electrostatic forces are prevalent in aqueous solutions (note that most of the liquids tested herein are nonaqueous). The electrostatic pressure contribution is always repulsive, but only relevant when ions are present. Liquids undergo molecular ordering and adhesion in the proximity of a hydrophilic surface and this effect is amplified in confinements whose size approaches the order of several molecular diameters leading to structural forces.[6] Denser packing of molecules equate to a liquid density increase in the associated region. Short-range solvation forces are prominent only within approximately a nanometer from an interface and decay rapidly, while long range solvation forces remain a controversial topic.[6] We only consider van der Waals forces in this analysis. The van der Waals forces across several thin film systems may interact with one another (overlapping force fields) due to their close proximity in a nano-confinement.

The theoretical extent of van der Waals forces from a surface is generally reported as several tens nanometers (hundreds of Angstroms) and this extent is typically divided into non-retarded and retarded zones. Retarded forces are also referred to as Casimir forces and decay faster than non-retarded forces.[7] [8] Retardation effects occur when confined molecules are relatively far enough apart that their dipole moments become out of phase faster than the electric field interactions between the molecules, which are limited by the finite speed of light.[9] Thus, retardation effects occur in only certain aperture or pore sizes. Theoretically, retardation effects occur at separation distances greater than 10 nm, but decay rapidly;[10] hence retarded forces are not felt in confinements smaller than this threshold and become negligible beyond the nanoscale. However, experimentally, Israelachvili and Tabor observed that retarded forces are found in planar apertures above 50 nm,[9] while Boström et al. found non-retarded forces in apertures as small as 3 nm.[11] An important variable in the description of van der Waals forces is the Hamaker constant, A_H, an interaction constant (with units of Joules) that is unique for each thin film system and that takes into account molecular interactions and the number density of molecules in the solids/fluids surrounding the film.[12] Specifically, calculations of A_H account for induction, orientation, and dispersion van der Waals forces. A_H values allow molecular interactions to be considered from a continuum perspective and are dependent on fluid and material properties. For an aperture of distance d, the non-retarded van der Waals force per unit area decays

as $1/d^3$ while the retarded van der Waals force per unit area decays as $1/d^4$; A_H usually values differ between these regimes.[9]

4. Approximation of Nanoscale Capillary Pressure in 3D

A 3D meniscus in a cylindrical pore of radius R ($D/2$) can be considered to be a series of local 2D meniscus film systems whose aperture height, S, changes with the radial distance, r, along the pore. S is determined by the length of a geometrical chord and the average of the disjoining pressure in the cylindrical pore renders $\bar{P}_c^{n,3D}$, the average 3D nanoscale capillary pressure, namely,

$$\bar{P}_c^{n,3D} \approx P_c^m - \frac{1}{R-h_{pre}} \int_0^{R-h_{pre}} \left(\frac{\int_{h_{pre}}^{(S-d_g)/2} \Pi_m(h,S)dh}{\frac{S-d_g}{2}-h_{pre}} \right) dr, \quad (S6)$$

with

$$S = 2\sqrt{R^2 - r^2} \quad . \quad (S6)$$

Per the Derjaguin approximation,[12] the local disjoining pressure of a curved surface with a certain film system and thickness is approximated by the disjoining pressure of a flat surface with the same film system. Using this approximation we integrate along the geometrical cords of the circular area. An estimate of $\bar{P}_c^n$ for a symmetric 3D meniscus with regions of constant and non-constant curvature in the presence of an adsorbed or precursor film of height h_{pre} and within a planar channel or pore space of height D is given by:

$$\bar{\Pi}_m = \frac{A+B}{6\pi\left(R-h_{pre}\right)} \quad (S7a)$$

$$A = \left[\left(\frac{-A_{123}}{2a^2} + \frac{A_{123}}{8(a-2)^2} + \frac{-A_{232}}{2(a-1)^2}\right)\left(\frac{R\left(\tan^{-1}\left(\frac{h_{pre}r}{\sqrt{h_{pre}^2-R^2}\sqrt{R^2-r^2}}\right)+\tan^{-1}\left(\frac{r}{\sqrt{h_{pre}^2-R^2}}\right)\right)+\sqrt{h_{pre}^2-R^2}\tanh^{-1}\left(\frac{r}{R}\right)}{h_{pre}R\sqrt{h_{pre}^2-R^2}}\right)\right]_{r=0}^{r=R-h_{pre}}$$

$$\ldots (S7b)$$

$$B \approx \left[\left(\frac{-A_{123}}{2} \right) \left(\frac{\sqrt{h_{pre}^2 - R^2}\left(\tan^{-1}\left(\frac{r}{\sqrt{R^2 - r^2}} \right) \right) + h_{pre}\tan^{-1}\left(\frac{h_{pre}r}{\sqrt{R^2 - r^2}\sqrt{h_{pre}^2 - R^2}} \right) - h_{pre}\tanh^{-1}\left(\frac{r}{\sqrt{h_{pre}^2 - R^2}} \right)}{h_{pre}^2 \sqrt{h_{pre}^2 - R^2}} \right) \right]_{r=0}^{r=R-h_{pre}}$$

$$\dots \text{(S7c)}$$

where $a = 1 - d_g/S$. The term B is approximate because we assume $h_{pre} \ll R$ for simplification purposes, a reasonable assumption for nano-confinements greater than 10 nm in diameter. Without this assumption the solution to the ODE is tediously long (that is, the above form is comparatively concise), but can be solved and displayed with a software such as Wolfram *Mathematica*.

5. Determination of Hamaker Constants for Retarded van der Waals Forces

Table S1. Retarded Hamaker constants for the experimental fluids

Fluid or Solid	B_{22} (10^{-28} J)	B_{123} (10^{-28} J)	B_{232} (10^{-28} J)
heptane	2.74	-1.92	2.74
methanol	25.64	11.37	25.64
decane	3.21	-1.84	3.21
isopropanol	23.23	9.65	23.23
Water	27.52	12.74	27.52
Acetone	23.91	10.13	23.91
Silica	7.94	---	---

Hamaker constants in the retarded regime differ from those in the non-retarded regime, are often denoted by B_H, and are calculated by:[9]

$$B_H = \hbar c \frac{\pi^2}{240} \left(\frac{\varepsilon_0 - 1}{\varepsilon_0 + 1} \right)^2 \phi(\varepsilon_0) \quad , \quad \text{(S8)}$$

where $\hbar$ is the reduced Planck constant, c is the speed of light, ε_0 is a medium's dielectric constant, and $\phi(\varepsilon_0)$ is a function whose value lies between 0 and 1 and is commonly taken to be $69/(2\pi^4)$.

6. Dimensionless Numbers Visual Diagram

Recall, we propose that a dimensionless number (designated by the Greek letter Λ) for the ratio of average surface forces over a meniscus (non-retarded and retarded van der Waals, electrostatic, etc.) to bulk capillary forces in an average or representative pore size will be useful in nanofluidics and nano-porous media:

$$\Lambda = \frac{\overline{\Pi}_m}{P_c^m} \quad . \text{ (S9)}$$

Also, a simple dimensionless index (designated by the Greek letter Γ) for assessment of when there is considerable change in effective pore diameter due to elastocapillary deformation is the ratio of the length of collapse to the length of the media or the imbibition length of interest, namely,

$$\Gamma = \frac{l_c}{L}. \text{ (S10)}$$
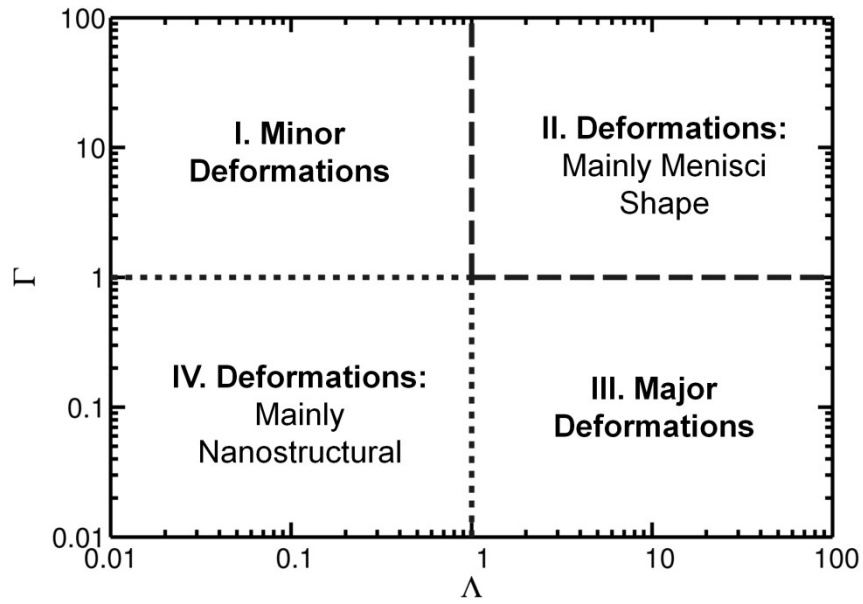
Figure S3. Conceptual diagram of the significance of the dimensionless numbers Λ and Γ. Researchers are encouraged to calculate estimates of Λ and Γ for their (nano)porous media of interest. If the values fall in region I then menisci and elastocapillary deformations are minor or even negligible and conventional imbibition and multi-phase flow predictions should not falter. If the values fall in region II then the material is strong enough or relevant length of fluid travel is small enough that elastocapillary effects are small, but the effects of surface forces (depending on the solid and fluid types and pore sizes) on meniscus shape are significant. Likewise, if the values fall in region IV, nanostructural deformations are prevalent. In both of these regions some deviation from conventional imbibition and multi-phase flow predictions is anticipated. In region III major nanostructural and menisci deformations converge leading to a severe deviation from conventional imbibition and multi-phase flow predictions (such as seen in the data presented in this paper). These region-wise descriptions hold best the farther values are from the borders of a region.

7. Menisci Shapes in 1D Nano-Slits

The nanochips' low aspect ratio microchannel pathways were intended as fluid conduits to the 2D nanochannel arrays in the center of the chips and acted as fluid reservoirs. Though the focus of the study was on the 2D nanochannels, unusual lateral shapes of the imbibition fronts within these channels prompted ancillary analysis.

The low aspect ratio microchannels leading to the arrays of 2D nanochannels are fundamentally nano-slits. The nano-slits are 1000 nm high, on average, and 80 μm wide and each slit channel is composed of varying material surfaces and channel heights. The structure of the nano-slits allows an examination of bulk capillary curvature in the lateral direction, interface stability, and film flow actions in thin apertures of compound surface properties. The top material of the nano-slits is borosilicate glass and from the center to the edges of the channel the bottom materials are: platinum, ~1 μm below the borosilicate glass top; silicon dioxide, 1 μm below the borosilicate glass top; and, after a sharp step, silicon dioxide, 2 μm from the borosilicate glass top. This slit is connected to an adjacent high aspect ratio silicon dioxide microchannel via a 60 nm high aperture which runs along the channel geometry. Figure 1 of the manuscript displays a schematic visualization of the compound configuration. The platinum film, originally intended to be an electrode, spans approximately half of the total width of each nano-slit.

In the nano-slit aperture, $w>>h$ and, per Eq. S3, capillary pressure in the vertical direction dominates over that of the lateral direction. The result of this dominance is nontraditional menisci shapes in the lateral direction. Front speeds and lateral shapes of the menisci within the complex nano-slits differ greatly among the observed liquids; instability and unusual multi-curvatures are observed in many cases. Figure S4 displays images of the diverse lateral curvatures for several of the tested fluids. The vertical curvature of the menisci within the 1000 nm high aperture cannot be captured with 2D optical microscopy techniques. Methanol imbibed the swiftest into the nanofluidic chips, completely filling a nano-slit on the order of seconds. On the other hand, water struggled the greatest with imbibition into the nano-slits, moving slowly, on the order of minutes, with an erratic, multi-curvature interface. Interestingly, the lateral menisci of the hydrocarbons heptane and decane were also slow, and the profile was "V"-shaped instead of hemispherical or curved when the front was atop sections with the metal film. The extreme differences in the shapes of lateral menisci and imbibition progression between the different wetting liquids required a phenomenological explanation. Similar to the data obtained from the 2D nanochannels, the nano-slit imbibition trends do not correlate to the bulk physical properties listed in Table 1 of the manuscript.
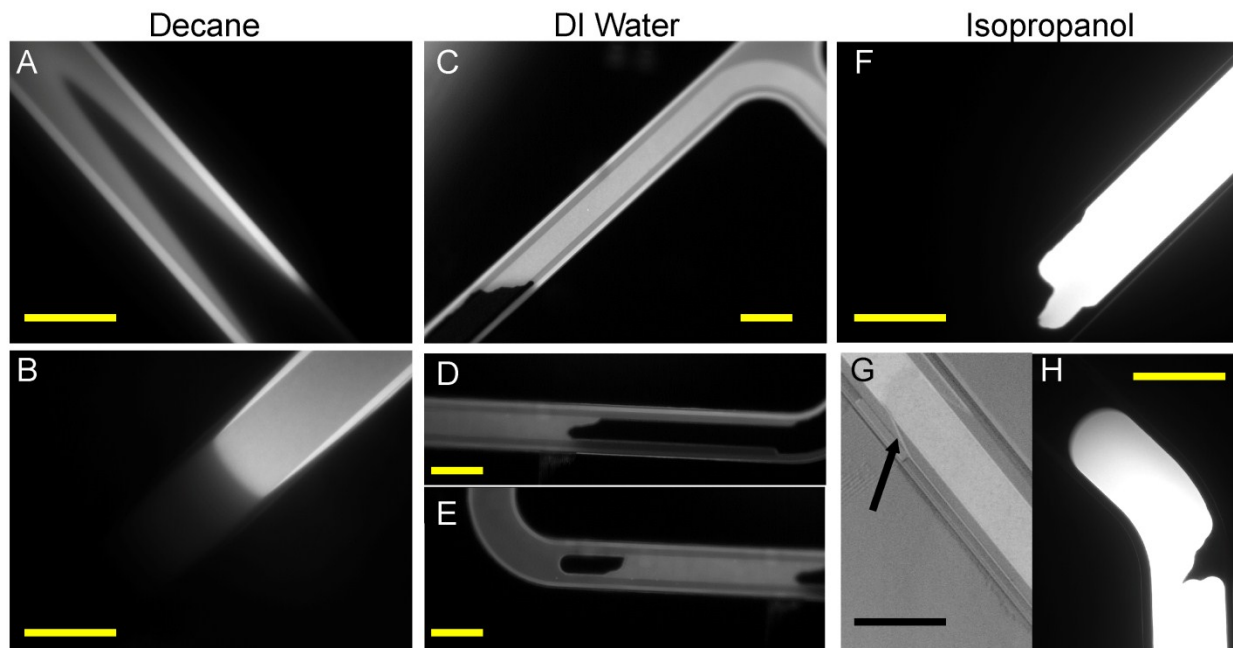
Figure S4. Imbibition situations in the nano-slits or low aspect ratio microchannels: (A) Decane imbibition front over a location where platinum is present. (B) Decane imbibition front over a location where no platinum is present (silica is under the front). (C) - (E) DI water forms a wavy, unstable front on all microchannel materials. The upper image is a dynamic meniscus while the lower two are static. (F) Isopropanol imbibition front over a location where no platinum is present. (G)-(H) Isopropanol imbibition front over a location where platinum is present taken with two different types of microscopy. Scale bars are all equal to 80 μm. All fluids are doped with Rhodamine B and images are captured with a Zeiss Axiovert 200M with the exception of Image (G) which features, for comparison, pure isopropanol and was captured with a Zeiss Axioskop 2 MAT.

Corroborative Phenomena in the Composite Nano-Slits

Liquid imbibition speed, interface shape and stability, and material preference are observed in the nano-slits. The unusual and varied lateral menisci in the nano-slits are firstly evidence of the complete domination of capillary pressure in the vertical direction over capillary forces in the horizontal direction along the width of the nano-slits. Thus, local capillary pressure can be approximated as the curvature between two plates. Regions of higher local capillary pressure move faster than adjacent regions and result in protruding areas of an interface front (for example, the middle of the parabolic isopropanol meniscus profile shown in Panels G and H of Figure S4). Liquid pressures behind the menisci in the nano-slits are also mathematically negative, on the order of -50 kPa while no cavitation is observed. Distorted menisci are reported in other works with nano-slits and are proven to be a product of suction due to negative pressure conditions in nano-slits with elastic membranes.[13] [14] [15] The inward deformation of the slits will theoretically lead to higher capillary pressures (in the limit of increased meniscus deformation) and higher imbibition velocities (in the limit of increased hydraulic resistance).

Fronts of isopropanol bound between glass and platinum indicate that capillary pressure is largest in the middle of the nano-slit. Indeed, the middle of an aperture is the location where suction deformation is

largest. Yet, not all of the observed lateral menisci share isopropanol's behavior. For example, the observed capillary pressure of decane and heptane between glass and platinum in a 1000 nm thick aperture is seemingly much less than that of the same liquids between silica and glass in a 2000 nm deep aperture (Panel A of Figure S4). Furthermore, the inferred capillary pressure of these hydrocarbons is the smallest in the middle of the slits for those wall compositions. The hydrocarbon meniscus may be subject to deformation at this location and/or the distorted channel appreciably increases the resistance to flow. Water, the tested liquid with the highest surface tension, had the most unstable interface, most likely due to pinning and propagation of resulting locally non-constant curvatures; isopropanol is observed to exhibit similar instabilities when bound between glass and silica in a 1000 nm thick aperture. Additionally, the liquid imbibition speeds negatively correlate with A_{232}, which indicates thinning of the air film enclosed by a meniscus in apertures as thick as 1000 nm high. Indeed, retarded van der Waals forces between various surfaces including glass have been measured out to separations of 1.2 μm.[6]

The above observations in the nano-slits further confirm that a complex interplay between metastable liquids and elastocapillary deformation and long-range intermolecular forces (as well as surface charges) must be considered within the experimental system in addition to conventional hydrodynamic and interface descriptions.

8. Additional Figures and Further Nanofluidic Observations of Interest
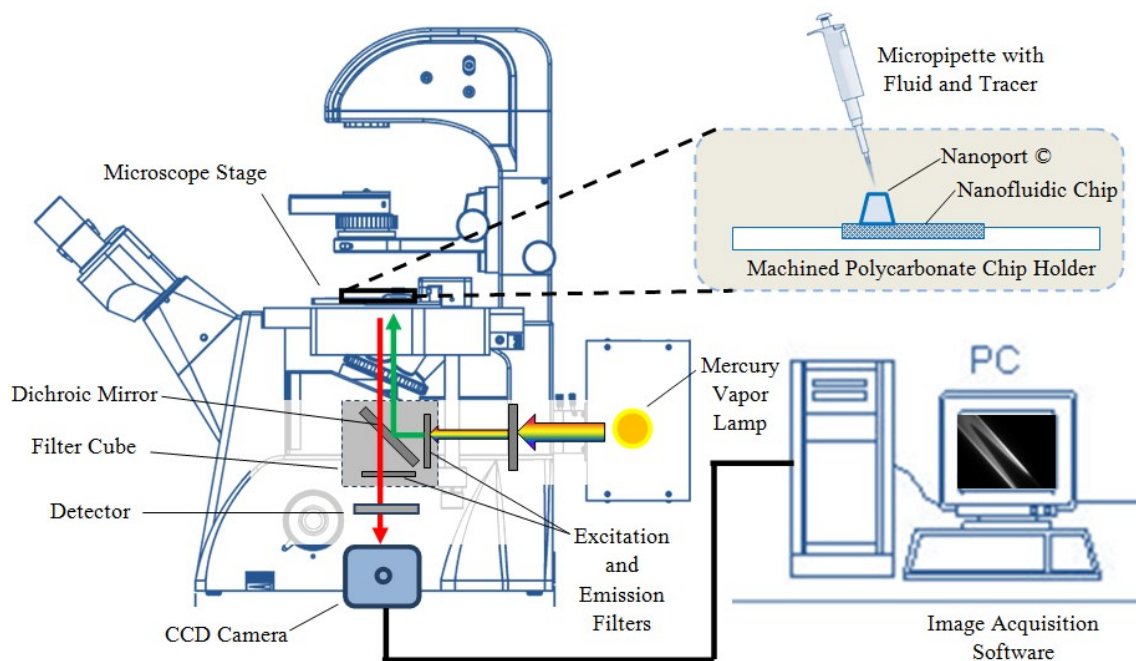
Figure S5. Diagram of the fluorescent microscope setup (Zeiss Axiovert 200M) used to capture data.

Inhibited imbibition due to high salt concentration

Aqueous solutions with high salt concentrations were introduced into the nanochannels several times. Figure S6 displays an example of the imbibition result of a 0.5 M NaCl solution doped with Rhodamine B. The results were difficult to compare to the pure liquids of the other sections because the imbibing fronts rapidly evaporated and "salted out/in" during imbibition. Per Raoult's Law, the vapor pressure of a pure solution is lowered when solute is added; hence, the solution is more likely to evaporate. Evaporation, like gas dissolution described in previous sections, is a <u>volume dependent</u> process and occurred rapidly in the nanochannels while the microchannels remained saturated. As displayed in Figure S6, evaporation in the small isolated volumes of the unconnected nanochannels did not permit imbibition as far as 250 μm in even the largest nanochannel. Salting out/in occurs when the solubility of solute molecules (e.g., Rhodamine B) is reduced/increased in a solution of high ionic strength and the molecules precipitate as a function of salt concentration. The ionic strength of the solution is a positive function of salt concentration.
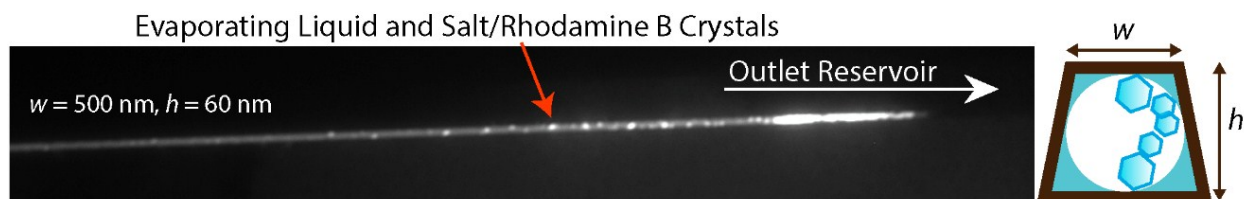
Figure S6. Evaporation and salting out of 0.5 M NaCl solution doped with Rhodamine B within a 500 nm × 60 nm channel.
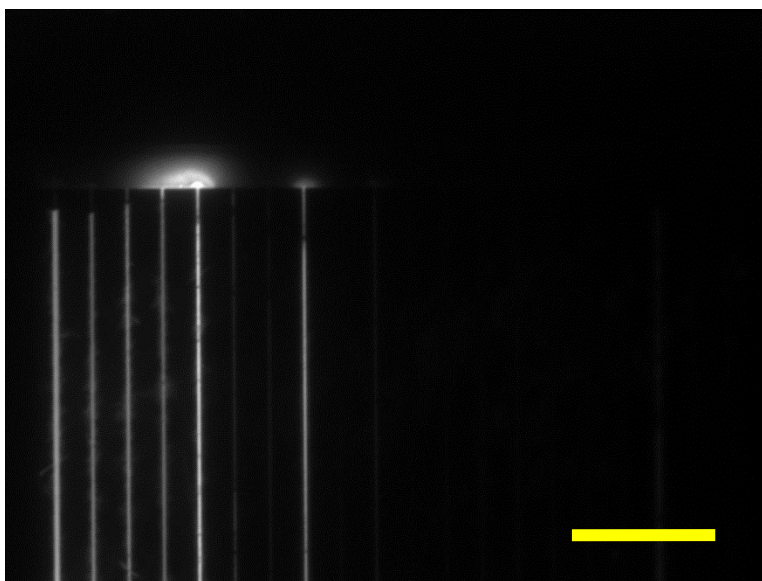
Figure S7. A fan like discharge of isopropanol emanates from some mid-sized nanochannels ($\geq$ 100 nm × 60 nm) while in others captured in this photo the meniscus front stops just short of the channel outlet; the yellow scale bar is 16 μm.
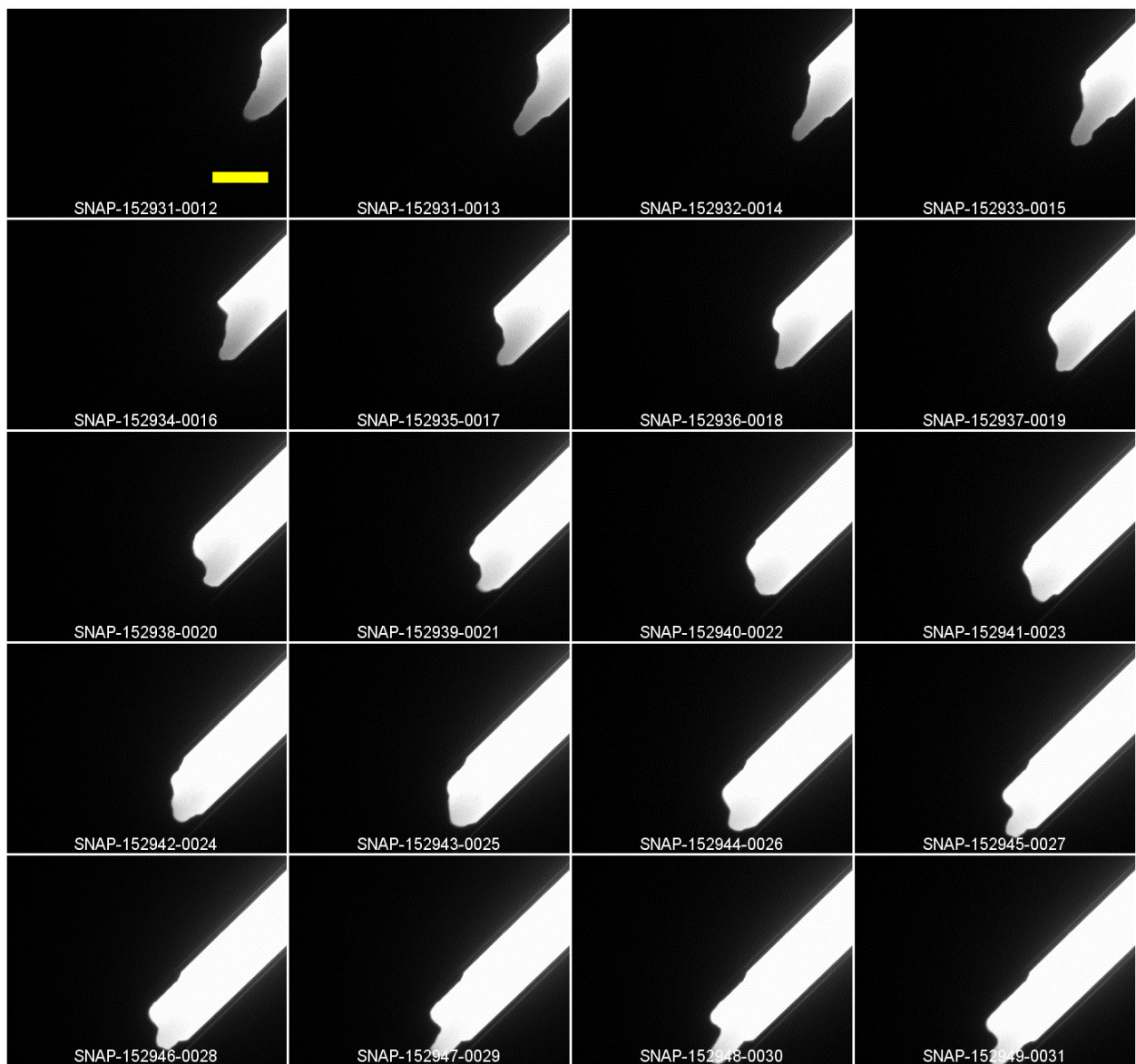
Figure S8. Dynamic visualization of a lateral isopropanol meniscus imbibing over silica in one of the nano-slits (low aspect mcirochannels); the yellow scale bar is 80 μm. The snapshots are presented in order from left to right and row by row, as indicated by the numbers at the end of the image names following the timecodes. The front is very unstable, but was stable on the platinum portions of the nano-slits (see Figure S4).
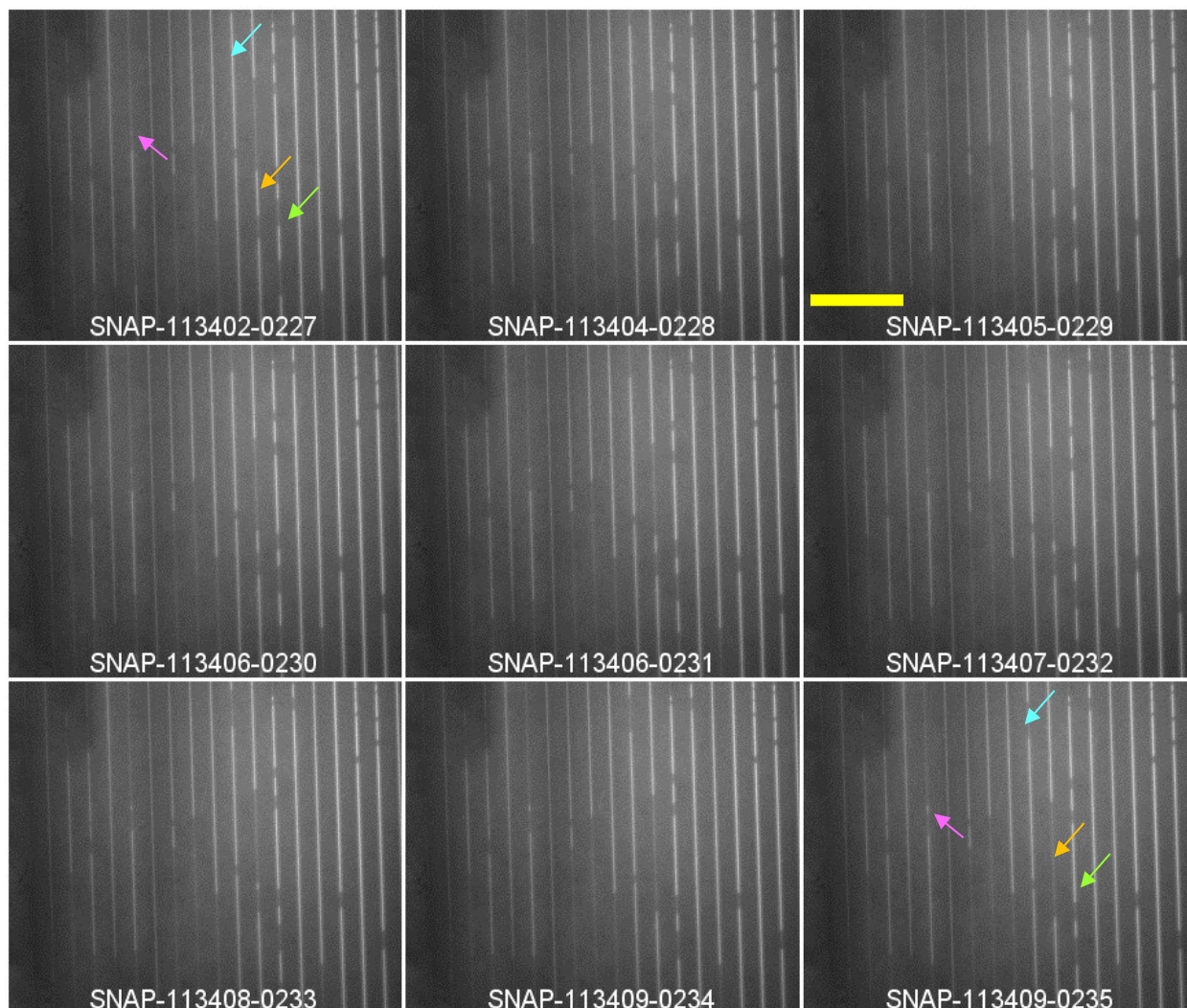
Figure S9. Images of gas slug movement in a compromised nanofluidic chip (compromised due to leakage between channels in very narrow apertures, as indicated by the faint background fluorescent signal); the yellow scale bar is 18 μm. The snapshots (part of a longer sequence of images) are presented in order from left to right and row by row, as indicated by the numbers at the end of the image names following the timecodes. Colored arrows indicate some areas of major changes in liquid/gas position between the first and last image. The movement and fairly constant (with time) shape of the gas slugs indicates that the liquid (isopropanol) is too saturated in gas (and tracer) for noticeable gas diffusion to occur. Also, the gas does not appear to flow in and out of the nearby apertures but the liquids do, indicating the apertures are mostly saturated in liquid. The arrows indicate areas where the nearby apertures source or extract liquid to and from the nanochannels (liquid plugs appear to "disappear" and "reappear"). An alternative interpretation to this interesting image stack is capillary condensation.

Crystallization of Thin Films in the Nanofluidic System

Dendrite ice crystals are found to form on the platinum in the nano-slits (or low aspect ratio microchannels) when the chips are subjected to mild winter temperatures upon transport between experimental facilities (no colder than 2˚C; the absolute minimum temperature for the applicable days of data collection). Dendrite ice crystals are natural fractal patterns that generally only form when air is supersaturated with water vapor and temperatures are within -10˚C to -20˚C.[16] However, some sources report that these fractal patterns can also form in the temperature range of -1˚C to -3˚C and low excess water vapor.[17] Supercooled water vapor may result in the nucleation of ice crystals within a thin film of water saturated in Rhodamine B. As the water freezes the fluorescent solute is excluded from the crystal phase. This mechanism explains the seemingly negative dendrite morphology in Figure S10 and S11. The platinum electrodes on the chips are assumed to be the site of ice nucleation because metals are superior conductors of heat. If ice only takes the dendrite morphology in the temperature range of -10˚C to -20˚C, the formation of these dendrites in thin water films suggest that the thermodynamic phase transition properties of the film and chip environment may differ from bulk properties and ambient conditions. Evidence of ice formation in the nanochannels at the 2˚C is also observed (see Figure S12). The crystallization occurred in the nanochannels hours before the nano-slits. As displayed in Figure S12, such crystallization was strong enough to compromise the structure of the silica nanochannels; this deformation occurred more prominently in the large nanochannels (left of Figure S12) than the smaller ones.
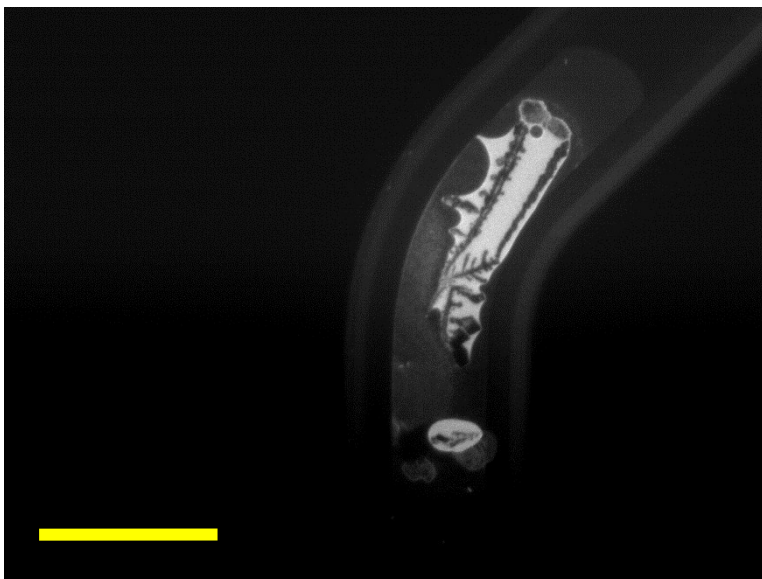
Figure S10. A dendrite crystal formed from DI water and Rhodamine B atop a platinum film in a nano-slit; the yellow scale bar is 80 μm.
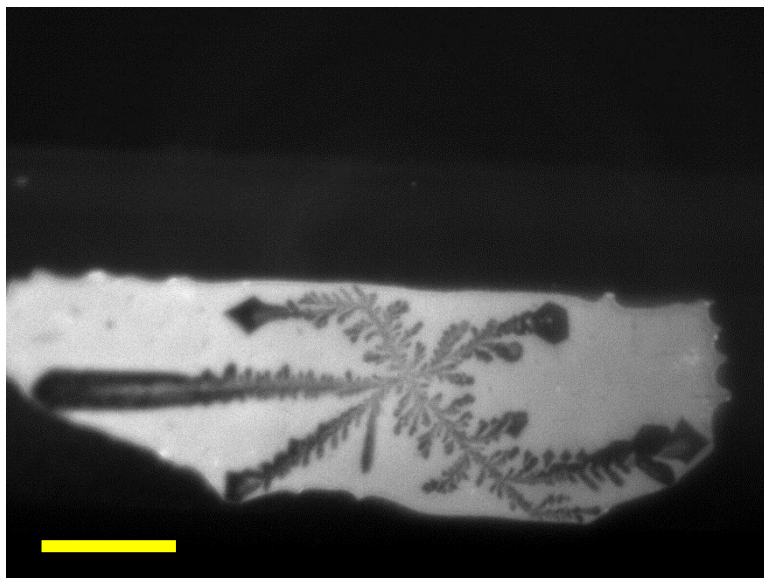
Figure S11. An elaborate dendrite crystal formed from DI water and Rhodamine B atop a platinum film in a nano-slit; the yellow scale bar is 16 μm.
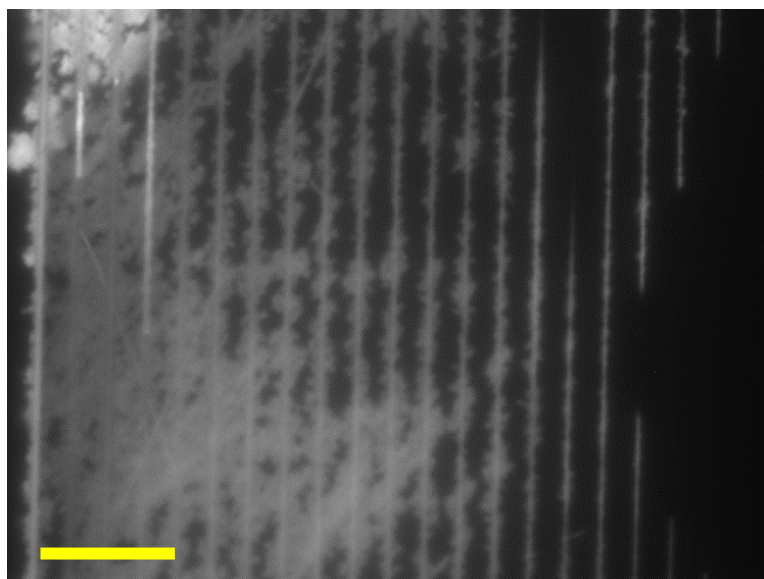
Figure S12. Crystallization in the nanochannels in which DI water and Rhodamine B compromised the structure and deteriorated the bond or structure of most of the channels (especially the leftward ones), as revealed by the signal of Rhodamine B; the yellow scale bar is 16 μm.

References

1 J. C. Berg, *An Introduction to Interfaces & Colloids: The Bridge to Nanoscience*, World Scientific, 2010.

2 W. van der Wijngaart, *Microfluid. Nanofluidics*, 2014, **16**, 829–837.

3 P. F. Man, C. H. Mastrangelo, M. Burns and D. T. Burke, in *, The Eleventh Annual International Workshop on Micro Electro Mechanical Systems, 1998. MEMS 98. Proceedings*, 1998, pp. 45–50.

4 R. B. Bird, W. E. Stewart and E. N. Lightfoot, *Transport Phenomena*, John Wiley & Sons, 2007.

5 B. V. Derjaguin, N. V. Churaev and V. M. Muller, in *Surface Forces*, Springer US, 1987, pp. 25–52.

6 J. N. Israelachvili, *Intermolecular and Surface Forces: Revised Third Edition*, Academic Press, 2011.

7 H. B. G. Casimir and D. Polder, *Phys. Rev.*, 1948, **73**, 360–372.

8 R. L. Jaffe, *Phys. Rev. D*, 2005, **72**, 021301.

9 J. N. Israelachvili and D. Tabor, *Proc. R. Soc. Lond. Math. Phys. Eng. Sci.*, 1972, **331**, 19–38.

10 H.-J. Butt, K. Graf and M. Kappl, *Physics and Chemistry of Interfaces*, John Wiley & Sons, 2006.

11 M. Boström, B. E. Sernelius, I. Brevik and B. W. Ninham, *Phys. Rev. A*, 2012, **85**, 010701.

12 B. V. Derjaguin, N. V. Churaev and V. M. Muller, in *Surface Forces*, Springer US, 1987, pp. 85–149.

13 L. H. Thamdrup, F. Persson, H. Bruus, A. Kristensen and H. Flyvbjerg, *Appl. Phys. Lett.*, 2007, **91**, 163505.

14 N. R. Tas, M. Escalante, J. W. van Honschoten, H. V. Jansen and M. Elwenspoek, *Langmuir*, 2010, **26**, 1473–1476.

15 J. W. van Honschoten, M. Escalante, N. R. Tas and M. Elwenspoek, *J. Colloid Interface Sci.*, 2009, **329**, 133–139.

16 N. H. Fletcher, *J. Cryst. Growth*, 1973, **20**, 268–272.

17 P. V. Hobbs, *Ice Physics*, Clarendon Press, 1974.